

Optimization of corrugated-QWIPs for large format, high quantum efficiency, and multi-color FPAs

Kwong-Kit Choi ^{a,*}, Carlos Monroy ^a, Venkataraman Swaminathan ^a, Theodor Tamir ^b, Ming Leung ^b, John Devitt ^c, David Forrai ^c, Darrel Endres ^c

^a *US Army Research Laboratory, Adelphi, MD 20783, USA*

^b *Polytechnic University, Brooklyn, NY 11201, USA*

^c *L3-Cincinnati Electronics, Mason, OH 45040, USA*

Available online 13 November 2006

Abstract

Previously, we demonstrated a large format 1024×1024 corrugated quantum well infrared photodetector focal plane array (C-QWIP FPA). The FPA has a cutoff at $8.6 \mu\text{m}$ and is BLIP at 76 K with $f/1.8$ optics. The pixel had a shallow trapezoidal geometry that simplified processing but limited the quantum efficiency QE. In this paper, we will present two approaches to achieve a larger QE for the C-QWIPs. The first approach increases the size of the corrugations for more active volume and adopts a nearly triangular pixel geometry for larger light reflecting surfaces. With these improvements, QE is predicted to be about 35% for a pair of inclined sidewalls, which is more than twice the previous value. The second approach is to use Fabry–Perot resonant oscillations inside the corrugated cavities to enhance the vertical electric field strength. With this approach, a larger QE of 50% can be achieved within certain spectral regions without using either very thick active layers or anti-reflection coatings. The former approach has been adopted to produce two FPAs, and the preliminary experimental results will be discussed. In this paper, we also describe using voltage tunable detector materials to achieve multi-color capability for these FPAs.

© 2006 Elsevier B.V. All rights reserved.

PACS: 42.25.Fx; 73.63.Hs; 85.35.Be; 85.60.Gz

Keywords: Infrared detector; Quantum well; Light-coupling; FPA

1. Introduction

Quantum well infrared photodetectors (QWIPs) possess many advantages such as selectable detection wavelengths, high uniformity, low $1/f$ noise, and large substrates. On the other hand, drawbacks such as low quantum efficiency η and large thermal dark current I_d limit their utility in high temperature and high frame rate conditions. In order to improve the detector performance, one needs to increase η without increasing I_d , in which case an effective approach is to increase the detector light coupling efficiency. Previously, we introduced the corrugated-QWIP or C-QWIP

geometry, and fabricated a large format 1024×1024 focal plane array (FPA) [1]. For this initial FPA, we adopted a shallow trapezoidal geometry for its simpler processing steps. The theoretical η is thus limited to $\sim 15\%$ for each pair of inclined sidewalls. Nevertheless, the $8.6 \mu\text{m}$ cutoff FPA exhibited a high BLIP temperature of 76 K with $f/1.8$ optics. The high BLIP temperature is in part attributed to the smaller I_d by 63% for its smaller active volume. In this paper, we will discuss different approaches to obtain a larger η based on the C-QWIP geometry.

2. Detector figures of merit

Before focusing on a particular detector figure of merit, it is useful to understand the roles of each detector

* Corresponding author. Tel.: +1 301 394 0495; fax: +1 301 394 1746.
E-mail address: kchoi@arl.army.mil (K.-K. Choi).

parameter in a more global detector optimization. To this end, we choose an application as an example, in which one tries to detect an object at a distance [2]. The goal is then to increase the detection range r of the target. Its value can be deduced from the signal to noise ratio of an imaging system, where

$$\frac{S}{N} = \frac{\eta g \kappa L_{\text{tar}} A_{\text{tar}} A_{\text{opt}} \cdot \text{EoD} \cdot \tau_{\text{int}} / r^2}{\sqrt{2 g(N_b + N_d) + \sigma^2(N_b + N_d)^2 + N_r^2}} \quad (1)$$

In the numerator of Eq. (1), g is the photoconductive gain, κ is the atmospheric transmission, L_{tar} is the in-band target radiance, A_{tar} is the target cross-sectional area, A_{opt} is the optical lens area, EoD is the fractional energy on detector due to lens optical diffraction, τ_{int} is the integration time. In the denominator, N_b and N_d are respectively the number of photoelectrons and dark electrons collected in each frame time, σ is the residual nonuniformity (RNU) after correction, and N_r is the number of read noise electrons.

To evaluate r , we assume that $\kappa = 1$; N_b is generated by the heated optics; $N_b \gg N_d$ (i.e. BLIP); and the detection criterion is when $S/N = 4$. Under these conditions, the detection range is

$$r^2 = \frac{\eta g L_{\text{tar}} A_{\text{tar}} A_{\text{opt}} \cdot \text{EoD} \cdot \tau_{\text{int}}}{4 \sqrt{2 \eta g^2 \frac{A_d \pi L_{\text{opt}}}{1+4(f/\#)^2} \tau_{\text{int}} + \left(\sigma \eta g \frac{A_d \pi L_{\text{opt}}}{1+4(f/\#)^2} \tau_{\text{int}} \right)^2} + N_r^2} \quad (2)$$

where A_d is the detector area, and L_{opt} is the optics radiance. Eq. (2) is useful in evaluating the impact of each detector parameter. For example, when the temporal noise (represented by the first term under the square root) dominates, r is proportional to $\eta^{1/4}$ but is independent of g . If the spatial noise (represented by the second term) dominates, the range is independent of both η and g , but inversely proportional to $\sqrt{\sigma}$. Finally, if the detection is read noise limited, the range is directly proportional to $\sqrt{\eta g}$ and inversely proportional to $\sqrt{N_r}$.

A quantitative example is given below based on a hypothetical system specification listed in Table 1. In Fig. 1, we first show r as a function of η with fixed $g = 0.4$ and $N_r = 200 e^-$. The expected $\eta^{1/4}$ dependence is observed only when $\sigma = 0\%$. For a finite σ , the η dependence is reduced, and when σ is in the order of 0.1%, the range becomes essentially independent of η for $\eta > 0.1$. With a large σ ,

Table 1
Assumed system parameters

Target size	25 cm × 25 cm	Detector size	25 μm × 25 μm
Target temperature	300 K	Integration time	5 ms
Optics diameter	5 cm	Optics temperature	400 K
$f/\#$	5	Optics emissivity	0.1
Detection wavelength	5–8 μm	EoD	0.1922

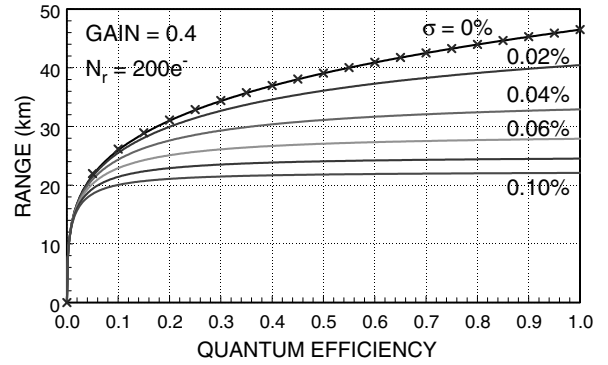


Fig. 1. The solid curves show r vs. η for different σ in 0.02% steps. The crosses represent $r = 46.5\eta^{1/4}$.

the detection is spatial noise limited and detection is independent of η as expected.

From Eq. (2), the effect of g seems to be very small unless there is a substantial read noise. We plot in Fig. 2 a range of g from 0 to 1 for fixed $\eta = 0.4$ and $N_r = 200 e^-$. The result confirms that as long as g is kept greater than 0.1, the range is practically independent of g . Even when g is as small as 0.05, r retains larger than 90% of its full range at $g = 1$. Only when g becomes extremely small, the read noise finally dominates, and the range decreases sharply. Incidentally, the conversion efficiency CE, which is the product of η and g , also changes in this example, and thus has the same effect as g . Therefore, without reference to η , CE alone cannot specify the detector performance.

In Fig. 3, we show the effect of read noise on r for $\eta = 0.4$ and $g = 0.4$. If the read noise is less than $500 e^-$, it will not affect the detection for any σ . Table 2 lists several specific examples. In Table 2, an ideal FPA with $\eta = 1$, $g = 1$, $\sigma = 0\%$ and $N_r = 0 e^-$ has a detection range r_{ideal} of 46.53 km. As long as $g \geq 0.4$ and $N_r \leq 200 e^-$, sets # 1–3 show that this range performance can be maintained. However, when σ increases from 0 to 0.02% in set #4, r is reduced to $0.87 r_{\text{ideal}}$. Reducing η from 1 to 0.5 in set #6 further reduces r to $0.78 r_{\text{ideal}}$. Finally, set #13 represents the typical QWIP FPAs currently available.

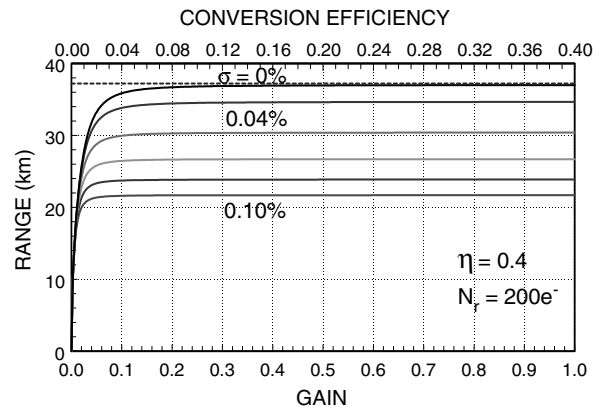


Fig. 2. The solid curves show r as a function of g for different σ in 0.02% steps. The dashed curve is an aid for viewing.

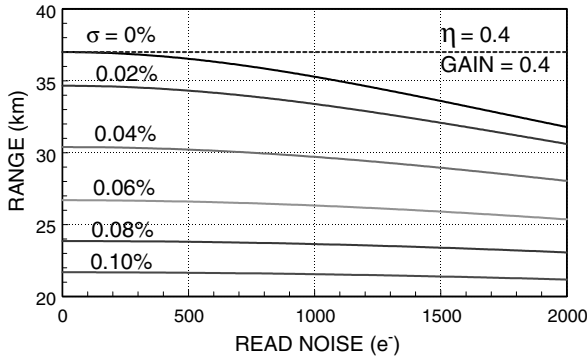


Fig. 3. The solid curves show r vs. n_{rd} . The dashed line is an aid for viewing.

Table 2
Range performance for different FPA parameters

Set #	η	g	σ (%)	N_r (e^-)	Range (km)	% of ideal range	Percentage of ideal range
1	1	1	0	0	46.53	100	██████████
2	1	0.4	0	0	46.53	100	██████████
3	1	0.4	0	200	46.49	99.9	██████████
4	1	0.4	0.02	0	40.47	87.0	██████████
5	1	0.4	0.02	200	40.45	86.9	██████████
6	0.5	0.4	0.02	200	36.09	77.6	██████████
7	0.4	0.4	0.02	200	34.60	74.4	██████████
8	0.4	0.2	0.02	200	34.44	74.0	██████████
9	0.4	0.2	0.02	500	33.39	71.8	██████████
10	0.4	0.4	0.04	200	30.37	65.3	██████████
11	0.4	0.4	0.04	500	30.22	64.9	██████████
12	0.4	0.2	0.04	500	29.71	63.9	██████████
13	0.1	0.2	0.05	1000	17.66	38.0	██████████

From this example, it is shown that the FPA performance is mostly affected by σ , followed by η , N_r and g . If one can achieve $\sigma \leq 0.02\%$, $\eta \geq 0.4$, $N_r \leq 200 e^-$ and $g \geq 0.2$, one could detect at $0.74 r_{ideal}$, which is twice the current value.

3. C-QWIP optimization

The above example shows that RNU is the most critical detector parameter. It is affected by a number of factors,

such as the detector material quality, the responsivity linearity, the FPA processing, and the light coupling uniformity. By choosing the matured $In_yGa_{1-y}As/Al_xGa_{1-x}$ As detector material system, high material quality is ensured. Responsivity linearity is closely related to the detector band bending under illumination. QWIP band structures are known to be unaffected by the presence of photons. Finally, the adoption of C-QWIP light coupling geometry avoids having fine grating structures in the pixels, which improves both the coupling and processing uniformity. Putting all these elements together will enable the production of highly uniform FPAs.

3.1. Large corrugation approach

The next important figure of merit is the quantum efficiency. To improve its value, the light coupling has to be more efficient. For the corrugated geometry, one approach is to enlarge its active volume, with which the entire pixel is occupied by a single corrugation. An example is shown in Fig. 4(a). The pixel has straight vertical sidewalls in the orthogonal direction. The top view of the fabricated pixels is shown in Fig. 4(b).

The original concept of corrugated coupling relies on total internal reflection (TIR) at the detector sidewalls. However, it turns out that the subsequent epoxy material that lies on top of the sidewalls can substantially reduce the internal reflection. Therefore, the present C-QWIP contains an MgF_2/Au cover layer for sidewall protection. This cover layer is electrically isolated from the top and bottom contacts of the pixels. The dielectric film MgF_2 is chosen for its high dielectric strength (breakdown voltage = 16 V for $t_d = 1000 \text{ \AA}$), low conducting current ($=1 \times 10^{-8} \text{ A/cm}^2$ at 6 V direct bias for $t_d = 4400 \text{ \AA}$), low refractive index, and small extinction coefficient.

To ensure that the sidewall retains its high reflectivity R , we calculated R as a function of the Au layer height t_m and MgF_2 layer height t_d . The calculation is based on the transfer matrix formalism applied to optical thin films having wavelength-dependent complex refractive indices N shown in Fig. 5. When $t_m < 600 \text{ \AA}$ in Fig. 6(a), optical tunneling through $MgF_2/gold$ layer and into the epoxy layer is possible although the incident angle is larger than the critical

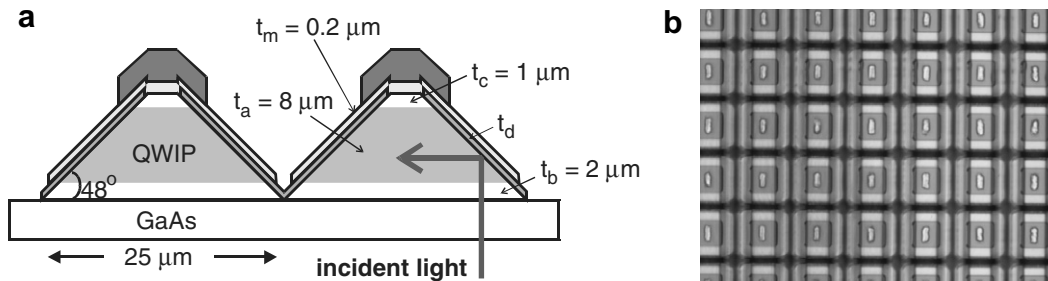


Fig. 4. (a) The side view of the C-QWIP pixels with $25 \mu m$ pitch. It has an active layer of thickness t_a , a top GaAs layer of height t_c , a bottom GaAs layer of height t_b , a MgF_2 layer of height t_d , a metal reflecting layer of height t_m , and an indium bump contact. (b) The top view of the pixels. The metal reflecting layer is electrically isolated from the top contact.

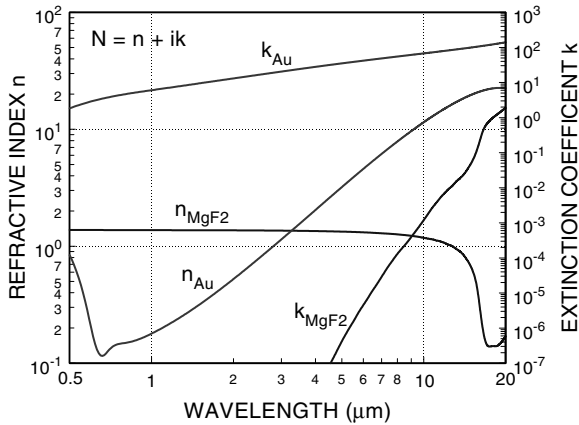


Fig. 5. The figure shows the complex refractive indices, $N = n + ik$, of MgF_2 and Au films as a function of wavelength.

angle. The resulting lower R is a case for the frustrated internal reflection. On the other hand, when t_d is small in Fig. 6(b), the excitation of surface plasmon polaritons in the gold surfaces at $\lambda = 0.54 \mu\text{m}$ gives rise to the so-called attenuated internal reflection. Between $0.7 < \lambda < 15 \mu\text{m}$, a small portion of the reflection is lost to ohmic heating in the gold metal via single particle excitation. When $\lambda > 15 \mu\text{m}$, phonon absorption in the dielectric is responsible for the reduction. The R minimum at $16.2 \mu\text{m}$ corresponds to the highest LO phonon energy in the MgF_2 layer.

The result in Fig. 6(a) shows that with an infrared absorbing epoxy, a gold layer of $t_m > 600 \text{ \AA}$ is needed to produce good optical isolation against the epoxy, with which $R > 0.98$ below $\lambda = 10 \mu\text{m}$. On the other hand, with an appropriate layer of gold, R is not very sensitive to t_d as shown in the insert of Fig. 6(b), and it is generally larger than 0.95. At a large t_d of $1 \mu\text{m}$, R becomes effectively unity within a wide wavelength range. TIR is thus restored in this thickness regime. Therefore, the present cover layer design is capable of providing good optical protection and good reflectivity.

Because Fig. 6(b) shows that the reflectivity R is negligibly affected by the optical losses, we have simplified our

calculations by replacing the gold film with a perfectly conducting layer when obtaining most of our results for the detector quantum efficiency. In Fig. 7, we show the corresponding rigorous modal transmission line (MTL) EM solution to the pixel geometry [3,4]. We have assumed unity substrate transmission and a typical imaginary dielectric constant ϵ_i of 1.0 for the effective vertical permittivity $\epsilon_v = \epsilon_r + i\epsilon_i$ in the quantum well region. With thin MgF_2 dielectrics ($t_d < 0.1 \mu\text{m}$), $\eta \approx 36\%$, which agrees with the result obtained from the ray tracing techniques under TIR. For a larger t_d , η is slightly reduced because of optical interference. We will return to this issue in a later discussion.

We have also calculated the QE originated from the two vertical sidewalls at the ends of the corrugations, and have found that $\eta = 7\%$. The total η from the four sidewalls is therefore 43%. If a small free carrier absorption is included, η becomes close to 50%. For this level of QE, the detection range can be as high as $0.77r_{\text{ideal}}$. Judging from sets #4 and 6 in Table 2, increasing η beyond 50% will not improve the range performance significantly unless RNU assumes an extremely small value.

Note that although the value of η increases with the corrugation size, g is reduced at the same time because of the longer transit time across the thicker layers. Consequently, the conversion efficiency $\text{CE} = \eta g$, does not change appreciably. However, Fig. 2 above shows that g is not a significant factor in determining r , and a larger g , if necessary, can be obtained through material designs. For example, we have adopted QWIP structures with 106 quantum well periods, which is more than twice the usual number. By using an InGaAs well instead of a GaAs well, the Al molar ratio in the AlGaAs barriers can be lowered for the same cutoff wavelength. With the lower Al content, intervalley scatterings can be reduced, and the intrinsic g per period is larger. As a result, the measured g is 0.20 for a QWIP with $\lambda_c = 8.8 \mu\text{m}$ and is 0.30 for another QWIP with $\lambda_c = 11.6 \mu\text{m}$ at the bias of 4 V. An even larger g is observed at higher bias. Therefore, one can maintain a sufficiently large g in this approach.

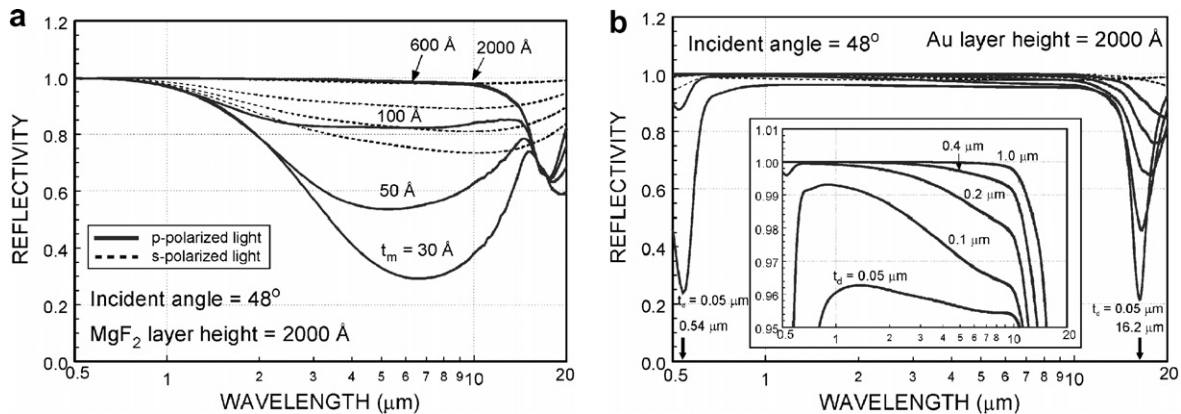


Fig. 6. The calculated sidewall reflectivity R for (a) different Au thicknesses and (b) different MgF_2 thickness, both with the assumed $N_{\text{GaAs}} = 3.24 + 0i$ and $N_{\text{epoxy}} = 2.25 + i$. The inset in Fig. 6(b) shows R in a larger scale.

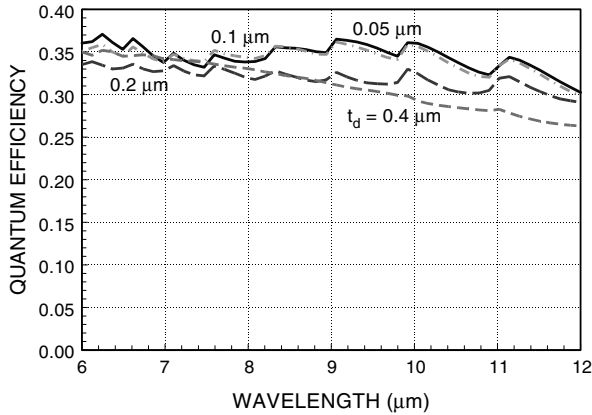


Fig. 7. The value of η calculated by using a rigorous EM theory for the detector geometry shown in Fig. 4. The substrate transmission is assumed to be unity.

If a large CE is desired (e.g. a large N_r), t_a can be reduced while keeping the geometry the same. This increases t_c and t_b accordingly. With the same reflecting surface, the reduction of η is slower than the increase of g , which results in a larger CE. Fig. 8 shows the calculated η contours for different t_c and t_b while keeping the total thickness the same. The dashed lines are the t_c and t_b combinations that give constant t_a . Varying along a dash line, a maximum η can be obtained for a given t_a (i.e. a given g). For example, if $t_a = 5.0 \mu\text{m}$, one can choose $t_c = 3.2 \mu\text{m}$ and $t_b = 2.8 \mu\text{m}$, with which $\eta = 29\%$. This η is 1.34 times lower than the detector with $t_a = 11 \mu\text{m}$, but g will be 2.2 times larger. As a result, CE increases by 1.64 times. Another advantage of having a thin t_a is a lower operating voltage.

3.2. Small corrugation approach

A large corrugation gives a large and constant QE It is therefore suitable for many applications including broad-

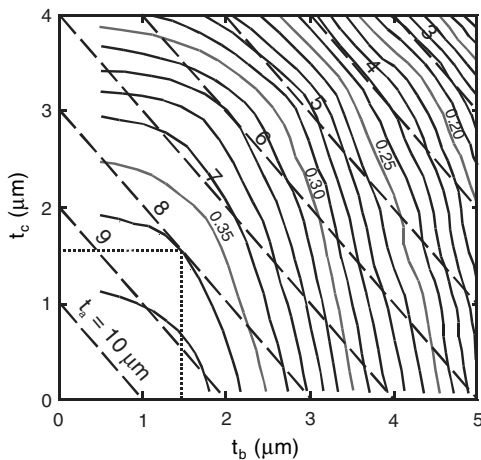


Fig. 8. The QE contours for different t_c and t_b while keeping $t_c + t_a + t_b = 11 \mu\text{m}$ and $t_d = 0.1 \mu\text{m}$. The dashed lines are loci for constant values of t_a as indicated. The maximum η for a given t_a can be obtained at the tangential points such as that indicated for $t_a = 8 \mu\text{m}$.

band and multi-color detection. It will facilitate FPA production since the same pixel geometry can be used for different wavelengths. It also does not require completely removing the substrate for absorption enhancement or cross-talk reduction. However, it does require a higher operating voltage and an AR coating, and it does not provide a very large CE.

To achieve a large CE, one needs to increase QE in a thin layer of active material. For this purpose, we will show that the corrugations can serve as resonant cavities to increase the incident optical intensity. In such cases, one does not need a large volume for absorption. Actually, in order to maintain a high degree of optical coherence, the optical path length inside the cavity should be short. This approach thus prefers small corrugations and thin substrates. AR coatings are not needed. The detector schematic geometry is shown in Fig. 9, and a pixel can contain several corrugations.

To simplify the discussion, we assume the sidewall angle to be 45° instead of 48° . With this approximation, one can identify two sets of coherent interference, which are labeled as interference 1 and 2 in Fig. 9. In interference 1, the incident beam r_1 partially transmits into the substrate as r_3 . The light makes a round trip inside the corrugation and interferes with the reflected beam r_2 . If r_4 and r_2 interfere destructively, the substrate reflection will be reduced and r_3 will be strengthened. Upon more round trip interferences, the substrate reflection will be completely suppressed and the internal intensity is greatly enhanced, analogous to the usual Fabry–Perot resonances in parallel planes. The analogy exists because all the incident light has the same path length of $(2t_g + 2h + w) = (2t_g + p)$ in the corrugation between the two substrate reflections, independent of the incident location. They differ only in that the corrugated structure possesses another interference set (#2), in which r_1 interferes with another beam r_5 incident on the opposite sidewall.

Since there is a phase shift of π upon 45° internal reflection for the TM mode, the optical E vector switches direction at the inclined surfaces as depicted in Fig. 9. Therefore resonance for interference 1 occurs when the sum of the

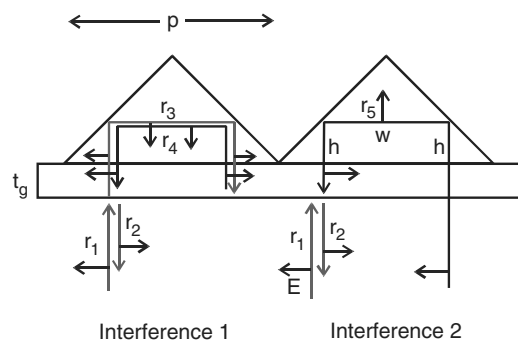


Fig. 9. Schematic C-QWIP geometry with period p and substrate thickness t_g . The figure also shows the ray diagrams of the two sets of optical interference.

phase shift of r_3 and r_4 is $2N\pi$, where N is an integer. Hence,

$$2\left(\frac{2\pi n_q p}{\lambda} + 2\frac{2\pi n_s t_g}{\lambda}\right) = 2N\pi, \Rightarrow \lambda = \frac{2n_q p + 4n_s t_g}{N}, \quad (3)$$

where λ is the wavelength in free space, n_s is the substrate refractive index, and n_q is the QWIP refractive index. For interference 2, following again the change of the E direction, the resonance condition is:

$$\frac{2\pi n_q p}{\lambda} + 2\frac{2\pi n_s t_g}{\lambda} = (2M + 1)\pi, \Rightarrow \lambda = \frac{2n_q p + 4n_s t_g}{2M + 1}, \quad (4)$$

where M is an integer. The resonant wavelengths for interference 1 are indicated in Fig. 10 by the arrows, and that for interference 2 are indicated by the bars. The structural parameters are: $p = 5.5 \mu\text{m}$, $t_a = 2.8 \mu\text{m}$, $t_c = t_b = 0 \mu\text{m}$, and $t_g = 1.2 \mu\text{m}$.

In Fig. 10, the calculated QE and the average internal intensity Φ_{in} with E component pointing vertically are calculated using the MTL model for the same p , t_a , and t_g but with 48° sidewalls, and the corrugations are covered with dielectric and metal where $t_d = 0.4 \mu\text{m}$. The MTL solution shows the same absorption peaks at similar locations. At $\lambda = 8.4 \mu\text{m}$ ($N = 6$), η can reach 50%. Since the active layer is now 2.9 times thinner than that of a large corrugation, CE is approximately 3 times larger than the previous large corrugation approach. The structure is thus able to serve as a resonant cavity for the incident field. The variation of the Φ_{in} ($\varepsilon_i = 0$) peaks is partially caused by the coincidence of the two interference sets whose electric fields tend to be out of phase.

For a $25 \mu\text{m}$ square pixel, there can be three corrugations in each pixel, with which $p = 8.33 \mu\text{m}$. Fig. 11 shows the MTL solution for this p value. The other parameters are: $t_g = 2.25 \mu\text{m}$, $t_d = 0.35 \mu\text{m}$, $t_a = 3.4 \mu\text{m}$, $t_c = 1.0 \mu\text{m}$ and $t_b = 0 \mu\text{m}$. The pixel has a large QE close to 50% at

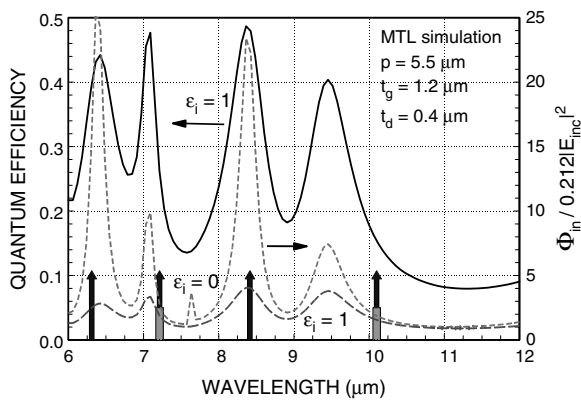


Fig. 10. The calculated QE (solid curve) and Φ_{in} (dashed curves) relative to the incident intensity as a function of wavelength. The arrows show the predicted resonant wavelengths for interference 1 (arrows) and interference 2 (bars) based on ray tracing techniques.

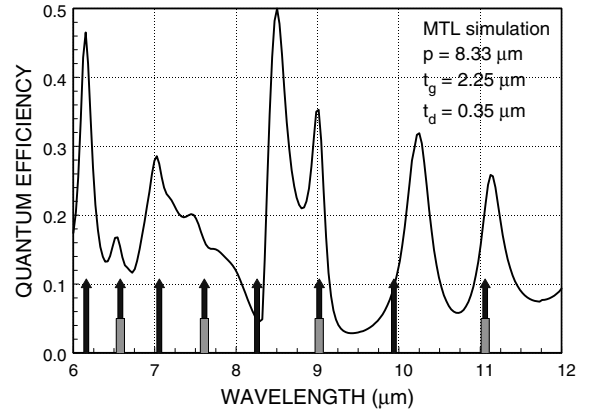


Fig. 11. The figure shows the calculated QE (solid curve) using MTL modeling [3,4]. The arrows show the predicted resonant wavelengths based on ray tracing techniques.

$\lambda = 6.2$ and $8.5 \mu\text{m}$. The corresponding N is 14 and 10, respectively.

Fig. 10 shows that Φ_{in} ($\varepsilon_i = 0$) at resonance can be 25 times stronger than the incident intensity inside the substrate. This C-QWIP approach has several advantages over the grating coupling. First, since resonance occurs within a single corrugation, the effect will not depend on the number of corrugations in each pixel. Second, the same corrugation geometry can be used for different wavelengths, and only the substrate thickness t_g needs to be adjusted to achieve the desirable path length. Third, one does not need a smaller p to detect a shorter λ , so that submicron electron beam lithography can be avoided. Fourth, the relatively large corrugation period produces less cross-talk among different pixels. Fifth, multiple wavelengths can be in resonance at the same time, thus producing multi-color coupling. By judiciously tuning p , t_g and N , any two resonant wavelengths can be selected to be arbitrarily close to the desirable wavelengths.

Finally, we point out that not all even N resonances produce a large QE. Furthermore, the peak positions are predicted somewhat differently by the MTL model and the ray-optics model. A major reason stems from the presence of the dielectric/metal cover, which is neglected in the ray-optics model but accounted for in the MTL model. Since the optical field can partially extend beyond the QWIP/dielectric interface and reaches the metal cover, the metal cover acts as a second but weaker resonant cavity, whose path length is lengthened by $2t_d$. The metal cavity thus has a different set of resonant λ . The hybridization of these two cavity modes produces the irregular peak positions and absorption strengths. The reflection from the metal cover is also responsible for the QE dependence on t_d in Fig. 7.

4. Two-color C-QWIPS

Based on the large corrugation approach, we have fabricated two FPAs with different cutoff wavelengths. The experimental result will be described in the next section.

Here, we will describe an approach to achieve a large format, high QE and two-color FPA. It is based on combining the corrugated geometry with a voltage tunable QWIP material. The detection wavelength of the FPA is controlled by the bias polarity. This approach has several advantages. First, with multi-color coupling capability of the C-QWIPs, both colors can be equally sensitive. Second, the pixel geometry is the same for any combinations of wavelengths. The fabrication procedures will be common to all two-color FPAs, and is actually the same as the single color FPAs. Third, each pixel has only one top contact, which allows the same pixel size, resolution and production yield as the single color FPAs. The drawbacks of this approach are the need of a readout circuit with voltage switching capability and the displaced timing of the two colors by an integration time or a frame time.

4.1. Detector material structure

There are many QWIP designs that exhibit voltage tuning. A more flexible design [5–7] is given in Fig. 12, which shows the band diagram of a material unit cell. Each unit cell is separated by an energy relaxation layer (ERL) made of 2000 Å $n = 1 \times 10^{18} \text{ cm}^{-3}$ GaAs as in Fig. 13. The entire structure contains a number of unit cells sandwiched

between two contact layers. In each unit cell, there are two superlattices (SLs), labeled SL1 and SL2, each of which absorbs at a specific wavelength, λ_1 and λ_2 , respectively. The SLs are joined by a graded barrier. This graded barrier blocks the conduction of the ground minibands but allows the electrons in the second miniband to go through. Each SL can be designed and optimized independently, which gives rise to its flexibility. The quantities λ_1 and λ_2 can be chosen to have any value within a wide range of wavelengths. The example below is designed for 4.3/8.8 μm MW/LW detection. The material layer parameters are shown in Fig. 12.

When a negative bias is applied to the substrate as in Fig. 13(a), which is on the left of the unit cell, the MW photoelectrons generated in SL1 pass through the graded barrier and change the impedance of the unit cell. The LW photoelectrons generated in SL2 pass into the highly conducting ERL, resulting in no impedance changes. The ERL is designed to attenuate the energy of the SL2 photoelectrons, so that these electrons will not be able to change the impedance of the next unit cell. Consequently, the detector only detects in the MW. When the bias polarity is reversed as in Fig. 13(b), only the SL2 LW photoelectrons pass through the graded barrier and produce an impedance change. The voltage tunability is thus achieved.

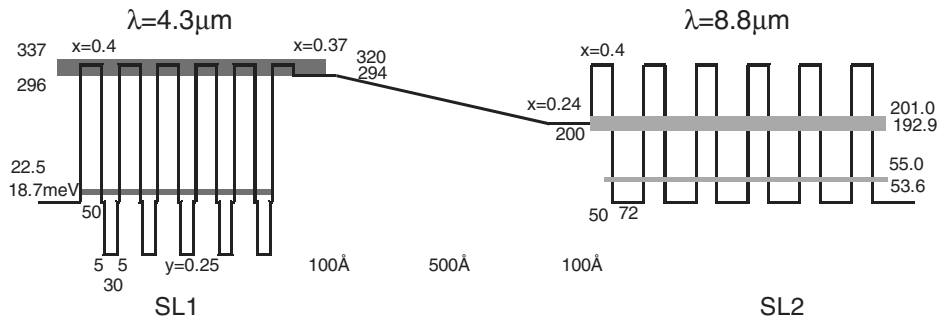


Fig. 12. The band diagram of a unit cell of a voltage tunable two-color detector.

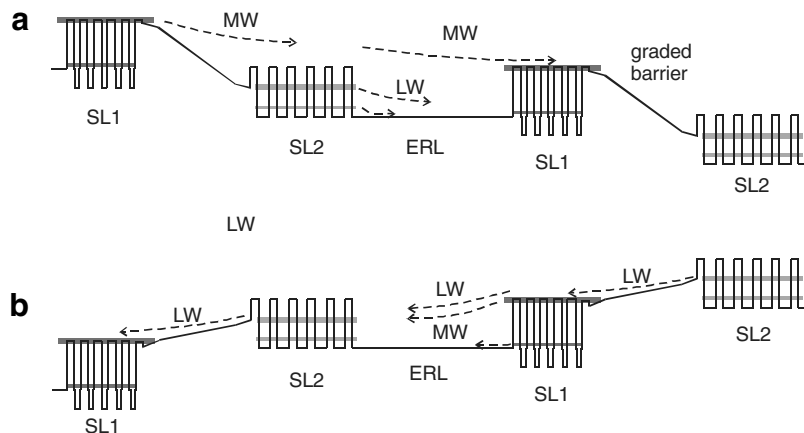


Fig. 13. The band diagram of the voltage tunable detector under (a) negative and (b) positive substrate bias. The arrows show the hot-electron trajectories. These hot-electrons originate either from thermal excitation or from photoexcitation.

4.2. Detector properties

Fig. 14 shows the measured spectral responsivity of a $p = 8 \mu\text{m}$ C-QWIP, which contains 7 two-color unit cells. The detector detects only the MW under negative substrate bias and only the LW under positive bias. There is no spectral cross-talk in both polarities. Fig. 15 shows the dark current density J_d and the window photocurrent density under $f/2$ optics. The detector is BLIP around 90 K under MW operation and around 65 K under LW operation. Further improvement can be made through material and light coupling optimizations. Two-color MW/LW detection can be achieved by incorporating such a detector material in a C-QWIP FPA.

To provide a more in-depth understanding of the detector characteristics, Fig. 16 shows the gain of the detector deduced from the noise measurement, in which the $g-r$ noise expression, $i_n^2 = 4egI_d$, is assumed, where i_n is the current noise per $\sqrt{\text{Hz}}$, and I_d is the dark current at a particular temperature. Under a negative bias and with $T < 116 \text{ K}$, g can be large and approaches 0.8 at large V . This large g indicates that the thermal electrons from the MW SLs are able to pass through the ERLs and traverse through almost the entire detector active thickness as Fig. 13(a) illustrated. In this bias polarity, the applied field is added to the built-in field of the graded barrier and thus increases the electric field inside the barrier. The MW thermal electrons are accelerated by this intense field and acquire a large energy so that they can overcome the energy attrition in the ERL regions. On the other hand, the thermal electrons from the LW SLs under this bias polarity do not pass through this high field region and thus do not have a similarly large energy. Since they cannot pass through the next graded barrier, they do not contribute to the dark current flow either.

In contrast, when a positive substrate voltage is applied, the applied field is mostly used to cancel the built-in field of the graded barrier as shown in Fig. 13(b). Therefore, the thermal electrons from the LW SLs do not gain as much energy in the graded barriers and thus may not be able to pass through as many unit cells. The observed

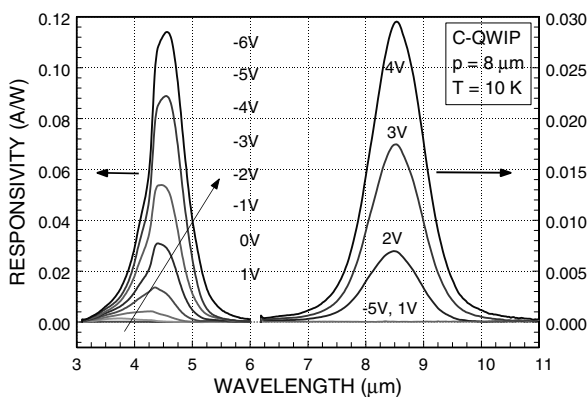


Fig. 14. Experimental responsivity of a single C-QWIP with $p = 8 \mu\text{m}$.

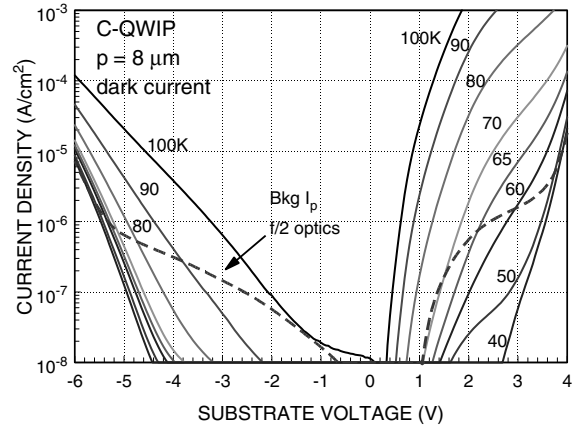


Fig. 15. The dark current (solid curves) and the background photocurrent (dashed curves) with $f/2$ optics.

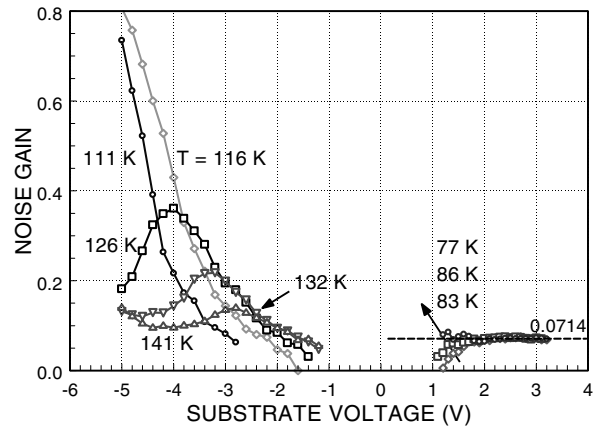


Fig. 16. The deduced noise gain from the measurement by assuming the $g-r$ noise expression $i_n^2 = 4egI_d$. Under positive bias, g is a constant when $V > 1.5 \text{ V}$.

g (≈ 0.0714) under positive bias is indeed smaller. The constant g value suggests that the mean free path of the LW thermal electron is a constant in this voltage range. If we assume that the LW electrons can only go through one unit cell and there is no statistical fluctuation in the mean free path, the noise would be that of the shot noise, where $i_n^2 = 2eI_d$ in each unit cell. Since the present detector consists of 7 (independent) unit cells connected in series, the noise current should then be given by $i_n^2 = (2eI_d)/7 = 4e(0.0714)I_d$. The fact that such constant g value is observed confirms the assumption that the thermal electrons from a LW SL cannot pass through a single ERL within 3.2 V bias.

In short, the detector is governed by $g-r$ noise under negative bias and by shot noise under positive bias for the present detector design. Since both η and g are constant under positive bias, the responsivity should also be a constant in this polarity, similar to a photodiode. However, the responsivity is observed to increase linearly with V between 1.5 and 4 V as shown in Fig. 17. This bias dependence is attributed to the increase of the tunneling

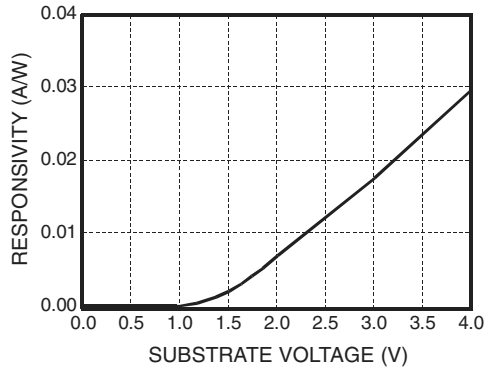


Fig. 17. The responsivity of the two-color detector at the peak wavelength under positive bias.

probability of the photoelectrons. In this detector design, the LW photoelectrons need to tunnel through the last (truncated) SL barrier before entering into the graded barrier. Changing the SL structure will change this bias dependence.

With the measured responsivity R , g and J_d , the dark current limited detectivity $D^* = R/(4egJ_d)^{0.5}$ can be calculated. For the MW, D^* is 2.4×10^{11} cm $\sqrt{\text{Hz/W}}$ at -4.5 V and 80 K. For the LW, D^* is 6.0×10^{10} cm $\sqrt{\text{Hz/W}}$ at 3 V and 60 K.

4.3. Energy relaxation layer design

In this two-color detector design, the electron energy relaxation layer plays an important role. It enables the selection of colors based on the bias polarity. If this layer is absent, under positive bias, the MW photoelectrons may inject into the graded barrier of the adjacent cell, and produce a MW signal in addition to a LW signal. Ideally, the ERL should reduce the energy of the unselected electrons sufficiently to avoid spectral cross-talk but yet allow the higher energy selected electrons to go through for a larger gain. It is relatively simple to design the layer under MW detection because the two types of photoelec-

trons have a large energy separation as shown in Fig. 13(a), but it is more difficult under LW detection when the two are much closer as in Fig. 13(b). In the latter case, one may need to accept a small LW gain by stopping all the high energy electrons, as in the present example, or accept some degree of spectral cross-talk for a higher LW gain by allowing most LW photoelectrons and some MW photoelectrons to go through. The design of the ERL is to obtain a suitable energy relaxation for a given application.

In GaAs, an electron loses its energy predominantly through optical phonon emission and plasmon emission [8]. Since plasmon scattering rate increases with the electron doping density, one can adjust both the ERL thickness and the doping to achieve a certain level of energy attrition. Fig. 18 shows the LW photoelectron energy distribution in the ERL under negative bias (Fig. 13(a)) for the present ERL parameters and the MW photoelectron distribution under positive bias (Fig. 13(b)). For the LW photoelectrons, only a small percentage of electrons remain ballistic after going through the entire ERL. For the MW photoelectrons, the layer is shown to be less efficient. About 1/3 of the electrons still remain in the ballistic peak. But since the present SL2 barrier structure imposes a high barrier for the hot-electrons with its third miniband at 365–400 MeV, the present ERL is adequate in reducing the high energy tail of the injected population. This example also shows that the SL1 and SL2 structures will also affect the ERL design.

From Fig. 18, the deduced scattering lifetime for the LW electrons is 0.078 ps while that for the MW is 0.17 ps. The higher LW scattering rate is due to the slower group velocity of the electrons. It turns out that both the phonon and plasmon scattering matrix elements are inversely proportional to the momentum of the electrons, which produces the calculated result. The momentum dependent scattering rate explains the large gain observed in Fig. 18 under negative bias. Since the MW electrons increase their momenta in the high field region before they are injected into the ERL as depicted in Fig. 13(a), the ERL is relatively transparent to these high energy electrons.

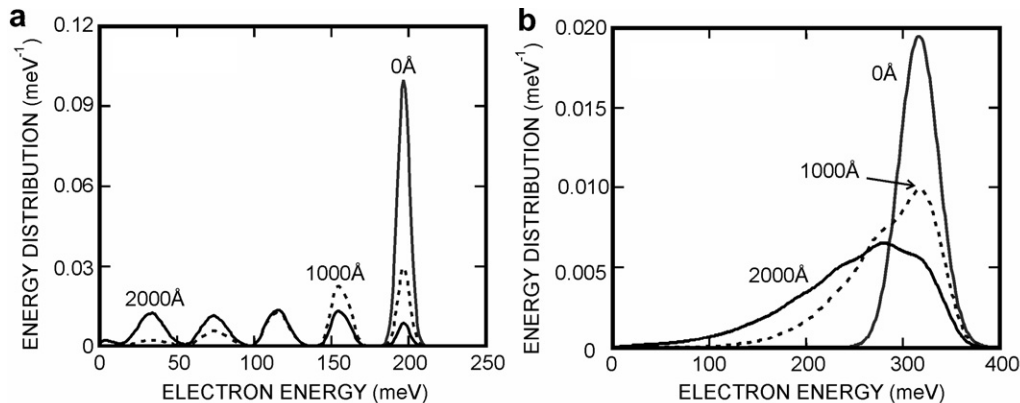


Fig. 18. The electron energy distribution when the electrons passing through the energy relaxation layer at 0 Å, 1000 Å and 2000 Å. The hot-electrons are either injected from (a) the LW SL (SL2) or (b) the MW SL (SL1).

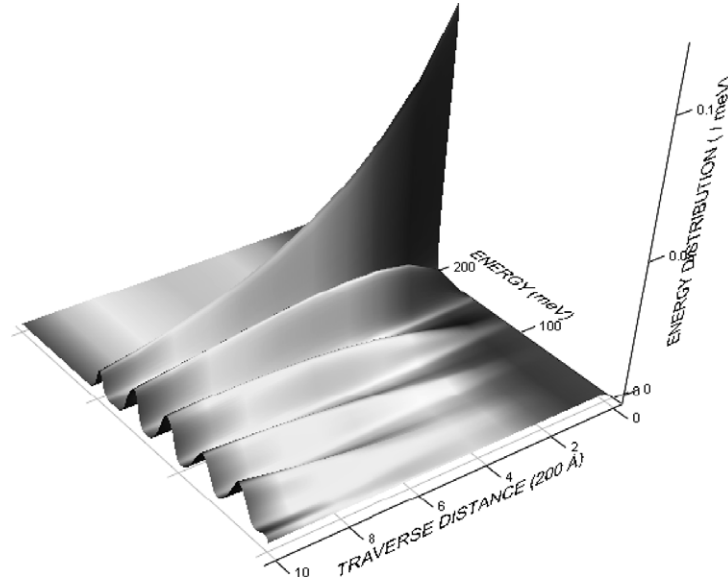


Fig. 19. The 3D plot of the hot-electron energy distribution as a function of traverse distance in the energy relaxation layer.

Fig. 19 is a more detailed plot of the evolution of the hot-electron distribution in the LW case. This plot shows the exponential decay of the injected population (with a decay constant of 0.078 ps) and the subsequent rise and fall of the lower energy replicas. The first replica below the injection peak first rises exponentially as each injected electron emits either a phonon or a plasmon and falls into this lower energy state. Its population eventually falls when it receives fewer electrons from the higher energy states than losing them to the lower energy states. Eventually, the electron distribution is given by the Fermi-Dirac distribution in thermal equilibrium. Since plasmon emission with 1×10^{18} doping is about 1.73 times faster than phonon emission [8], the replicas are separated by an energy closer to the plasmon energy (43.5 meV) than the optical phonon energy (36.3 meV).

5. FPA performance

In this section, we will describe the single color FPA performance based on the large corrugation approach. The FPAs are in 1024×1024 format with $25 \mu\text{m}$ pixel pitch. The first wafer material, labeled as LC1, contains 106 periods of 5 \AA GaAs/ 40 \AA $\text{In}_{0.1}\text{Ga}_{0.9}\text{As}$ / 5 \AA GaAs/ 700 \AA $\text{Al}_{0.21}\text{Ga}_{0.79}\text{As}$ active material sandwiched between two contact layers. The QW region is doped with $n = 9 \times 10^{17} \text{ cm}^{-3}$. The second wafer material, labeled as LC2, has the same layer structures as LC1 except that the barrier layers are made of $\text{Al}_{0.12}\text{Ga}_{0.88}\text{As}$. The wafers were first wet etched to $11 \mu\text{m}$ deep to create the inclined sidewalls. They were then dry etched to create the other two vertical sidewalls. Subsequent steps were depositing top and bottom ohmic contacts and depositing optical reflectors. The finished pixel geometry is shown in Fig. 4(b). The selected die was then hybridized to

CE031A ROICs at L3-communications Cincinnati Electronics (L3-CE). The ROIC has 13 Me^- charge capacity and was modified to provide detector bias larger than the nominal value of 1 V.

The detector materials were first characterized using large area, edge coupled detectors. From the responsivity and noise gain measurements, the absorption coefficient of the materials for parallel propagating light can be deduced. Based on the geometrical model, the quantum efficiency η of the present C-QWIP geometry can then be calculated. The result is shown in Fig. 20. The grown materials have cutoffs at 8.3 and $11.6 \mu\text{m}$ for the LC1 and LC2 structures, respectively. They are shorter than the nominal 9 and $15 \mu\text{m}$ cutoffs based on the 67% rule for conduction band offset. These discrepancies indicate either a calibration difference or a low level of p-type doping in the barriers, which can give rise to a higher barrier height. As a result, the LC1 detectors are bound state detectors, although the LC2 detectors remain to be extended state detectors.

Due to the bound excited states, η of LC1 approaches η_{abs} calculated in Section 3 only at large bias. At -13 V , η is equal to 28% without an AR-coating. With a suitable AR-coating, η can be 38%, which is consistent with the prediction in Fig. 7. Due to the extended nature of the LC2 excited states, η becomes independent of bias above -4 V , and its value is as expected. Below -4 V , the excited states are better characterized as the localized, resonant states of the wells. The necessary transitions from these states to the free propagating states in the barriers reduce η from the value of η_{abs} .

The corresponding FPAs were characterized at L3-CE. Fig. 21 shows the signal output in digital units under different blackbody radiations. For the LC1 FPA, a fit to the data with the known g of 0.048 at -3 V yields

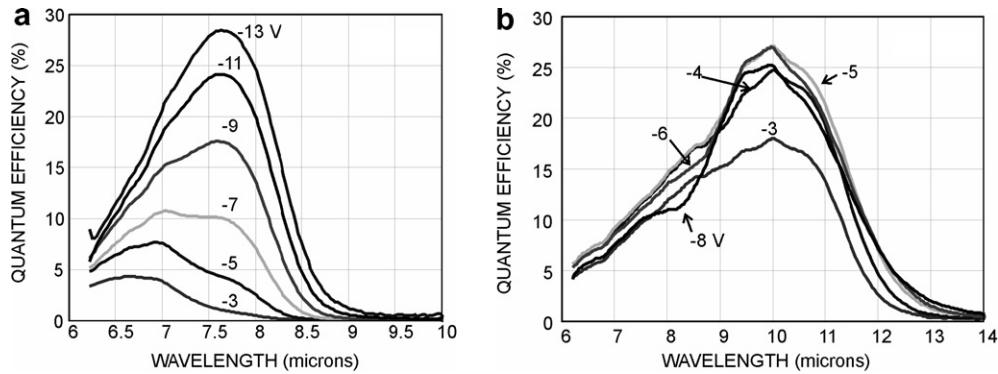


Fig. 20. The expected values of η of (a) LC1 and (b) LC2 at different substrate bias based on radiometric and noise measurements on large area edge coupled detectors. No AR-coatings are assumed.

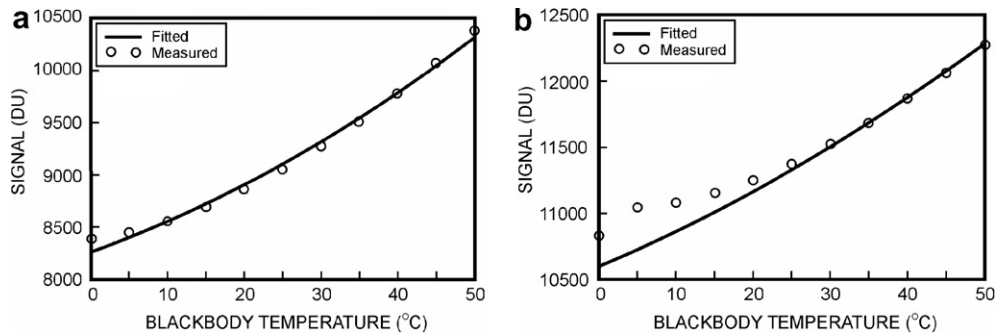


Fig. 21. The digital counts obtained from (a) the LC1 FPA at -3 V and 80 K and the digital counts obtained from (b) the LC2 FPA at -2 V and 68 K, both under a blackbody source.

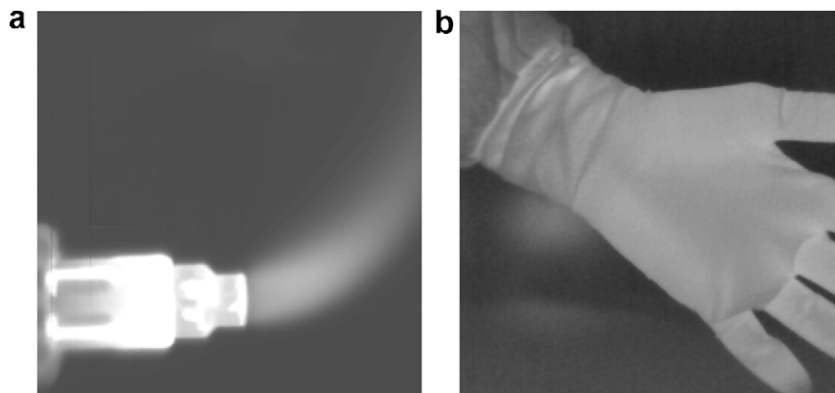


Fig. 22. (a) The image of a torch flame taken by the LC1 FPA at 80 K and (b) the image of a hand in glove taken by the LC2 FPA at 68 K.

$\eta = 7.1\%$. This value is somewhat larger than the 4.5% expected from Fig. 20(a). The extra QE may be attributed to the coupling contribution from the vertical sidewalls, which is not accounted for in Fig. 20. Due to limitation of the present ROIC, the FPA could not be biased to higher voltages to yield a larger η . Similarly, for the LC2 FPA, the fitting with $g = 0.16$ yields $\eta = 14.2\%$ at the highest achievable bias of -2 V. This η is also larger

than the 10% expected from the linear extrapolation of the data in Fig. 20(b). Therefore, the FPA performance at this tested bias regime is fully consistent with the single detector results, and thus indicates that with a more suitable ROIC, a larger η should be realizable. Fig. 22(a) and (b) show the infrared images obtained from the LC1 FPA at 80 K and 16 ms and from the LC2 FPA at 68 K and 0.3 ms, respectively.

6. Conclusion

In this paper, we have discussed the impact of different detector parameters on the detection range. The most critical figure of merit is the pixel uniformity, followed by the quantum efficiency, the read noise and finally the gain. We have described two corrugated geometries that can produce large format and high quantum efficiency FPAs. Large corrugations provide ample active material for large absorption, while small corrugations provide resonant cavities for large field enhancement. When this coupling scheme is combined with a voltage tunable material, a two-color FPA can be produced, whose detection range can be twice the current value. We have also presented the preliminary results for two $1\text{ K} \times 1\text{ K}$ single color FPAs using the large corrugation approach. Although large quantum efficiency has not been demonstrated in these FPAs, the values obtained at the achievable biases are fully consistent with our model, and thus it holds promise for improvement with more suitable ROIC designs. The high operating temperatures of these FPAs attest to its advantage. Further efforts are underway.

References

- [1] K.K. Choi, C. Monroy, A. Goldberg, G. Dang, M. Jhabvala, A. La, T. Tamir, K.M. Leung, A. Majumdar, Jinjin Li, D.C. Tsui, Designs and applications of corrugated QWIPs, *Inf. Phys. Technol.* 47 (2005) 76.
- [2] L. LaCroix, S. Kurzius, Peeling the onion: an heuristic overview of hit-to-kill missile defense in the 21st century, *Proc. SPIE* 5732 (2005) 225.
- [3] L. Yan, M. Jiang, T. Tamir, K.K. Choi, Electromagnetic modeling of quantum-well photodetectors containing diffractive elements, *IEEE J. Quant. Electron.* 35 (1999) 1870.
- [4] K.K. Choi, K.M. Leung, T. Tamir, C. Monroy, Light coupling characteristics of corrugated quantum well infrared photodetectors, *J. Quant. Electron.* 40 (2004) 130.
- [5] C.C. Chen, H.C. Chen, C.H. Kuan, S.D. Lin, C.P. Lee, Multi-color infrared detection realized with two distinct superlattices separated by a blocking barriers, *Appl. Phys. Lett.* 80 (2002) 2251.
- [6] A. Majumdar, K.K. Choi, J. Reno, D.C. Tsui, Voltage tunable two-color infrared detection using semiconductor superlattices, *Appl. Phys. Lett.* 83 (2003) 5130.
- [7] J. Li, K.K. Choi, D.C. Tsui, Voltage tunable four-color quantum well infrared photodetector, *Appl. Phys. Lett.* 86 (2005) 211114.
- [8] K.K. Choi, QWIP: A Quantum Device Success, in: W. Goddard, D. Brenner, S. Lyshevski, G.J. Iafrate (Eds.), *Handbook of Nanoscience, Engineering, and Technology*, CRC Press, New York, 2003, pp. 9–20.